 https://doi.org/10.3311/PPci.44011

Periodica Polytechnica Civil Engineering, 70(2), pp. 698–716, 2026

Numerical Investigation of RC Beams with an Integrated Frictional and Elastomeric Seismic Device

Orkun Yılmaz[1*], Lal Oğuz[2]

[1] Department of Civil Engineering, Faculty of Civil Engineering, Yildiz Technical University, 171 Eski Londra Asfaltı Caddesi, 34220 Esenler, Istanbul, Türkiye
[2] Graduate School of Science and Engineering, Yildiz Technical University, Davutpaşa Mah. Davutpaşa Caddesi, 34220 Esenler, Istanbul, Türkiye
[*] Corresponding author, e-mail: yilmazo@yildiz.edu.tr

Received: 14 March 2026, Accepted: 03 June 2026, Published online: 18 June 2026

Abstract

In conventional seismic design, reinforced concrete (RC) frames are typically detailed to form plastic hinges that dissipate seismic energy through inelastic deformation, but this strategy also leads to significant local damage under severe loading. Recent research has focused on low-damage strategies that shift inelastic demand from primary RC members to dissipative components. In this study, a frictional and elastomeric seismic device, originally developed for steel structures, was numerically integrated into an RC beam. Initially, the 3D nonlinear finite element modeling approach was calibrated against the load-deflection response of an experimentally tested RC beam from the literature. Subsequently, the calibrated modeling approach was used to evaluate the cyclic response of device-integrated RC beams. A parametric study was performed to investigate the influence of the friction coefficient, bolt pretension, and embedment configuration of longitudinal steel plates. Numerical results indicate that the device can substantially increase the cumulative energy dissipation capacity of the RC beam. When a single, short embedded longitudinal plate is used to transfer high resisting moments, severe strain localization is observed, leading to premature damage in the surrounding concrete. Using multiple embedded longitudinal plates distributes plastic deformations across a larger concrete volume, preventing the formation of a single dominant strain localization band and allowing the friction mechanism to maintain stable hysteretic behavior at larger drift levels. Although these findings are based on numerical analyses and require experimental verification, they support the concept as a promising solution for low-damage RC applications, provided that embedment detailing is carefully designed.

Keywords

reinforced concrete, frictional device, elastomeric device, low-damage seismic design, nonlinear finite element analysis, hysteretic behavior

1 Introduction

Reinforced concrete (RC) structures subjected to seismic loading are susceptible to significant damage in their main load-carrying members. In conventional seismic design of RC frames, plastic hinges are intentionally formed at the beam-end regions, allowing earthquake-induced energy to be dissipated through inelastic deformation of both concrete and reinforcement [1]. While this approach ensures global ductility, it also leads to considerable local damage, residual deformations, and degradation of structural components. As a result, the reparability of RC structures following seismic events is limited, and immediate re-occupancy is generally not possible without substantial repairs [2].

To overcome these limitations, recent developments in performance-based seismic design have focused on damage control strategies that transfer inelastic demand from primary structural members to dedicated, replaceable, and repairable components. In this context, fuse-type energy dissipation systems have been proposed to localize damage within sacrificial elements, thereby maintaining the integrity of the main structure. In the field of RC, several studies have investigated low-damage connection concepts based on this approach. For example, Soydan et al. [3] introduced fuse-type mechanical couplers for precast RC beam-column joints, demonstrating that seismic energy can be dissipated through controlled plastic deformation

Cite this article as: Yılmaz, O., Oğuz, L. "Numerical Investigation of RC Beams with an Integrated Frictional and Elastomeric Seismic Device", Periodica Polytechnica Civil Engineering, 70(2), pp. 698–716, 2026. https://doi.org/10.3311/PPci.44011

of the couplers instead of plastic hinge formation in the beams. Their nonlinear numerical analyses verified stable hysteretic behavior and increased energy dissipation capacity at large drift levels. Colajanni et al. [4] studied friction-based hybrid joints for RC frames and found that frictional interfaces at the joint region effectively dissipate seismic energy while reducing damage in concrete members. Both experimental and numerical investigations confirmed the stability and reparability of these systems. Qu et al. [5] examined precast prestressed RC joints with controlled yielding steel elements and observed reduced residual deformations and more balanced cyclic responses under repeated loading. A further study by Sonda and Pollini [6] also showed that concentrating damage in replaceable components may improve seismic performance and reduce irreversible damage in RC members.

Compared to the limited number of studies focused on RC structures, fuse-type energy dissipation systems have been extensively developed and validated for steel structures, where they are widely used as an effective seismic protection strategy. Early investigations into structural fuses established that concentrating inelastic deformation within sacrificial steel elements can enhance ductility and energy dissipation, while protecting beams and columns from severe damage [7, 8]. Yielding steel fuses with optimized geometries, including slit plates, butterfly-shaped elements, and hourglass-shaped links, have demonstrated stable hysteretic behavior, high energy absorption, and controlled post-yield stiffness [9–12]. Numerous experimental and numerical studies have confirmed that geometric optimization is essential for preventing premature buckling and improving the cyclic performance of steel fuses [13–16].

Friction-based fuse systems have also been widely implemented in steel structures as alternative or supplementary energy dissipation mechanisms. In these devices, seismic energy is dissipated through controlled sliding, which is governed by the friction coefficient and clamping force, resulting in stable hysteresis with limited strength degradation [17–20]. Experimental studies on both symmetric and asymmetric friction dampers, including those utilizing brake pads and sprayed aluminum interfaces, have demonstrated reliable cyclic performance and straightforward post-earthquake replacement [21–24]. Parametric studies have indicated that the friction coefficient and the level of bolt pretension have a significant effect on slip initiation, energy dissipation capacity, and overall system stability [25, 26].

In recent years, hybrid fuse systems that combine yielding, frictional, and elastic or self-centering mechanisms have been developed to achieve multi-stage energy dissipation and improved control of residual drifts in steel frames. Investigations of hybrid and replaceable fuse links integrated into beam-column connections have demonstrated increased seismic resilience, reduced residual deformations, and rapid post-earthquake repair capability [27–30]. These systems represent an advancement of the fuse concept, with the objective of balancing energy dissipation, stiffness control, and reparability through specifically designed mechanical interactions.

Although extensive research has been conducted on energy dissipation mechanisms in steel structures and there is increasing interest in low-damage RC connections, the direct integration of such dissipative devices within RC members remains insufficiently studied. Most applications in RC structures have focused on external devices or connection-level solutions, leaving the internal interaction between an integrated device and the surrounding concrete and reinforcement largely unexplored. In particular, devices combining friction-based dissipation with elastomeric components have received limited attention in this context, and the influence of embedment detailing on local damage distribution within the RC member remains an open research question.

The objective of the present study is to investigate the adaptation and integration of an existing frictional and elastomeric device, which was originally developed for steel moment-resisting frames by Yılmaz [31], into an RC beam. The device-integrated RC beam is intended to dissipate seismic energy within the device itself, thereby reducing the deformation demand imposed on the surrounding RC beam. The effectiveness of this integration was assessed solely through nonlinear finite element analyses using Ansys Mechanical 2024 R2 [32]. This study is therefore presented as a numerical feasibility assessment rather than a finalized or experimentally validated design methodology. The numerical modeling approach was first validated by reproducing the response of an experimentally tested RC beam from the literature. Subsequently, the cyclic responses of a bare RC beam and device-integrated RC beams were compared with respect to hysteretic behavior, energy dissipation capacity, plastic strain distribution, and force transfer among the internal components of the device.

2 Overview of the frictional and elastomeric seismic device

The frictional and elastomeric seismic device examined in this study was initially developed by Yılmaz [31] for application in steel structures. A patent for this device was registered

with Yılmaz and Bekiroğlu as inventors [33]. The device has been further improved and its configuration refined in subsequent research studies [34, 35]. The geometric configuration and main components of the device are illustrated in Fig. 1. The basic assembly consists of two outer plates, a central inner plate, friction members, elastomeric elements, a master pin, additional bolts, and stiffness members. An exploded view is provided in Fig. 1 (b) to clarify the internal mechanism and the arrangement of the dissipative core.

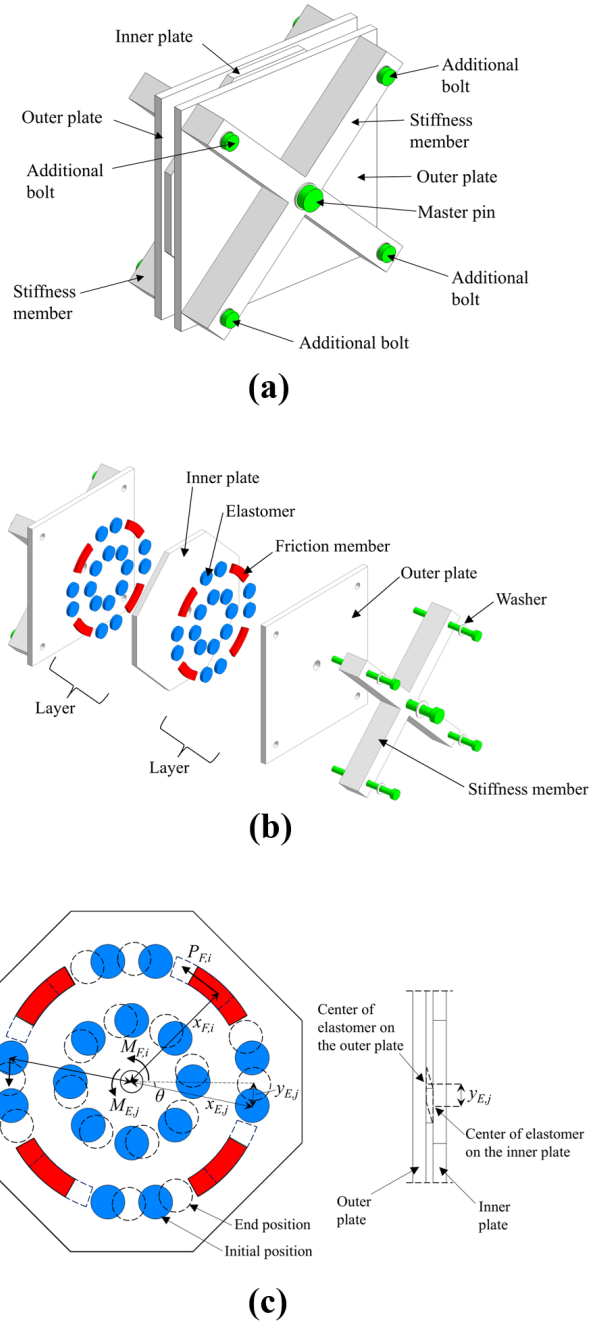

Fig. 1 The frictional and elastomeric seismic device: (a) General 3D view; (b) Exploded 3D view showing internal components; (c) Force distribution and mechanics of moment transfer

The interface comprising the friction members and elastomers, which is formed between each outer plate and inner plate, or between two adjacent inner plates when multiple inner plates are used, is referred to as a layer. In the configuration presented in Fig. 1, a single inner plate is placed between two outer plates, producing two layers (one on each side of the inner plate). The modular design of the device permits the addition of further inner plates to increase the number of layers as needed to achieve the required capacity.

The device is designed to allow rotation about the central master pin. Energy dissipation is primarily achieved through the friction members, which provide frictional resistance against the inner plate. The magnitude of this resistance is determined by the clamping force generated by pretensioning the master pin and the additional bolts. Although the friction members can be configured in various ways, optimization studies have indicated that arc-shaped friction members provide more stable cyclic performance than alternative geometries [31].

The mechanism of force transfer and moment generation within the device is illustrated in Fig. 1 (c). The total resisting moment of the device is derived from the combined contribution of the frictional resistance and the elastic moment contribution provided by the elastomers. The frictional moment (M_F) generated by the friction members is calculated as follows:

$$M_F = \mu T_F x_F, \tag{1}$$

where μ is the friction coefficient of the sliding interface, T_F represents the total pretension force applied to the bolts, and x_F is the effective distance from the center of rotation to the friction members.

The elastomeric components contribute to the moment capacity through their shear deformation. As the device rotates by an angle θ, each elastomer undergoes a tangential displacement ($y_{E,j}$), corresponding to the shear deformation across the elastomer thickness. The total moment contributed by the elastomers (M_E) is the sum of the contributions from the individual elastomers (j), as expressed:

$$M_E = \sum_{j=1}^{m} M_{E,j} = \sum_{j=1}^{m} \left(k_E y_{E,j} x_{E,j} \right) = \sum_{j=1}^{m} \left(k_E \theta x_{E,j}^2 \right). \tag{2}$$

In Eq. (2), m is the number of elastomers in a single layer, k_E is the shear stiffness of the elastomer, $x_{E,j}$ is the radial distance of the j-th elastomer from the center of the device, and $M_{E,j}$ is the moment contribution of the individual elastomer. The term $y_{E,j}$ represents the tangential displacement of the elastomer, which is linearly related to the rotation angle.

Finally, the total moment capacity (M_{dev}) of the device, accounting for the number of layers (n), is obtained by summing the frictional and elastomeric components:

$$M_{dev} = n\left[\mu T_F x_F + \sum_{j=1}^{m}\left(k_E \theta x_{E,j}^2\right)\right]. \quad (3)$$

3 Validation of the finite element model

All nonlinear finite element analyses in this study were carried out using Ansys Mechanical 2024 R2 software [32]. To verify the accuracy and reliability of the finite element model of the RC beam, the experimental study conducted by Arduini et al. [36] was used as the reference benchmark. The RC beam designated as "Beam A1", which served as the unstrengthened control specimen in that experimental program, was selected for the validation analysis.

The cross-sectional details, loading and boundary conditions of Beam A1 are presented in Fig. 2. The beam features a cross-section of 200 × 200 mm and is reinforced with two longitudinal bars of 14 mm diameter (ϕ14) in both the tension and compression zones. Shear reinforcement consists of 6 mm diameter stirrups spaced at 150 mm centers (ϕ6/150).

The finite element mesh was generated to capture the interaction between concrete and reinforcement, as well as the stress distribution within the beam. The concrete volume was discretized using SOLID185 elements, which are 3D 8-node solid elements. For the longitudinal reinforcement and stirrups, REINF264 discrete reinforcing elements were utilized. These elements are embedded directly within the SOLID185 base elements, allowing for the simulation of reinforcement behavior without the need for shared nodes, assuming a perfect bond between the steel and concrete. Based on a mesh convergence study conducted to ensure solution accuracy, a global element size of approximately 25 mm was adopted. The mesh configuration and the element types employed in the developed model are illustrated in Fig. 3.

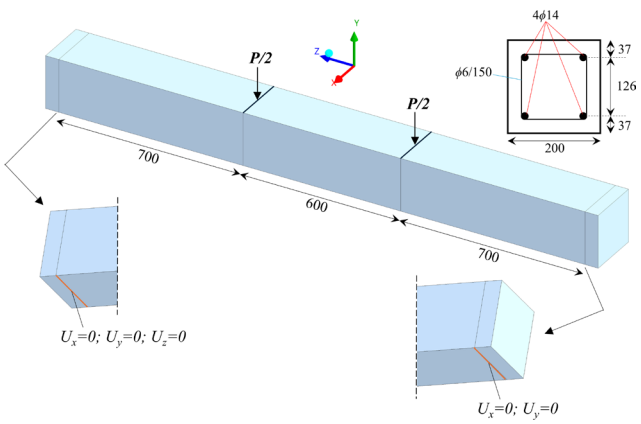

Fig. 2 The cross-sectional details, loading and boundary conditions of Beam A1

The Menetrey-Willam failure criterion, available in the Ansys library, was utilized to simulate the nonlinear behavior of the concrete. The compressive strength ($f_c' = 33$ MPa) tensile strength (f_t = 2.6 MPa), and Poisson's ratio (0.2) reported in the experimental study [36] were adopted directly. The remaining parameters required by the constitutive model, namely the biaxial compressive strength (f_{cb}), the dilatancy angle, and the post-peak softening parameters, were not specified in Arduini et al. [36] and were therefore determined through the calibration procedure. Exponential softening was adopted for both the compressive and tensile post-peak responses. The constitutive model for concrete and the calibrated parameter values are summarized in Fig. 4 and Table 1. For the steel reinforcement, a bilinear isotropic hardening model was adopted to represent plastic behavior. The mechanical properties were also adopted from Arduini et al. [36] as follows: elastic modulus (E_s) of 200 GPa, Poisson's ratio of 0.3, yield strength (F_y) of 540 MPa, ultimate strength (F_u) of 700 MPa, and an ultimate strain of 0.1.

Although the elastic modulus of concrete (E_c) was reported as 25 GPa in the experimental study, this value was adjusted during model calibration to 20 GPa. This adjustment accounts for the heterogeneous nature of concrete, micro-crack formation during testing, and deviations in the initial stiffness of the specimen. In addition, the parameters not specified in Arduini et al. [36] were calibrated against the experimental load-deflection curve. This calibration yielded a biaxial compressive strength of f_{cb} = 36.3 MPa (corresponding to 1.1 f_c'), a dilatancy angle of 12°, and the post-peak softening parameters listed in Table 1. The post-peak softening parameters were selected within the typical ranges reported for the Menetrey-Willam model and refined to ensure that the load-deflection response captured both the post-yield plateau and the overall load-carrying capacity observed experimentally.

The load *vs.* mid-span deflection curve obtained from the finite element analysis of Beam A1 is presented in Fig. 5,

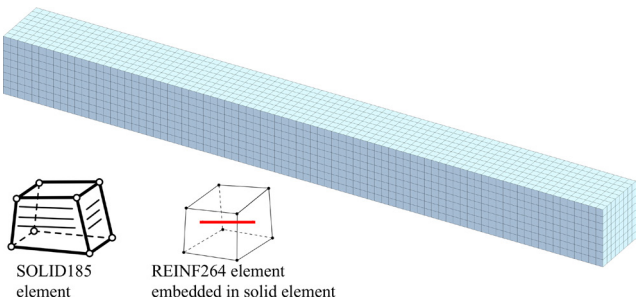

Fig. 3 Finite element mesh of the beam and details of the element types (SOLID185 for concrete and REINF264 for reinforcement)

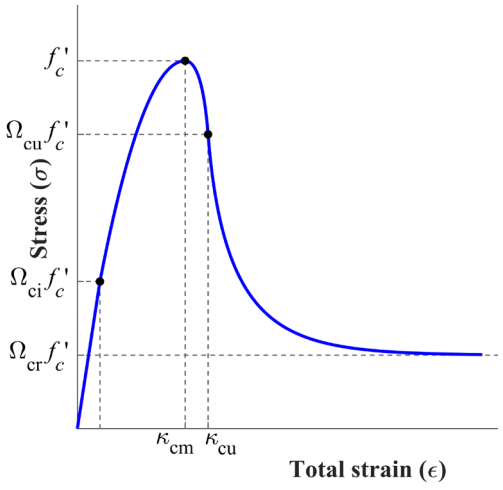

(a)

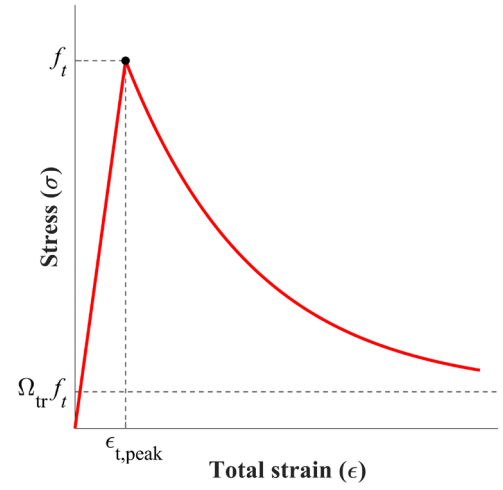

(b)

Fig. 4 The constitutive model for concrete: (a) Uniaxial compression; (b) Uniaxial tension

Table 1 Calibrated Menetrey–Willam material parameters for concrete

Parameter	Value
Plastic strain at uniaxial compressive strength (κ_{cm})	0.002
Plastic strain at transition from power law to exponential softening (κ_{cu})	0.0025
Relative stress at start of nonlinear hardening (Ω_{ci})	0.4
Residual relative stress at transition from power law to exponential softening (Ω_{cu})	0.8
Residual compressive relative stress (Ω_{cr})	0.2
Mode 1 area specific fracture energy (G_{ft}, N/m)	140
Residual tensile relative stress (Ω_{tr})	0.1

in comparison with the experimental results reported by Arduini et al. [36]. As shown in Fig. 5, the numerical model exhibits a high degree of agreement with experimental data. The calibration of the elastic modulus ensured that the initial stiffness of the model matched the actual beam behavior. Furthermore, the model successfully predicted

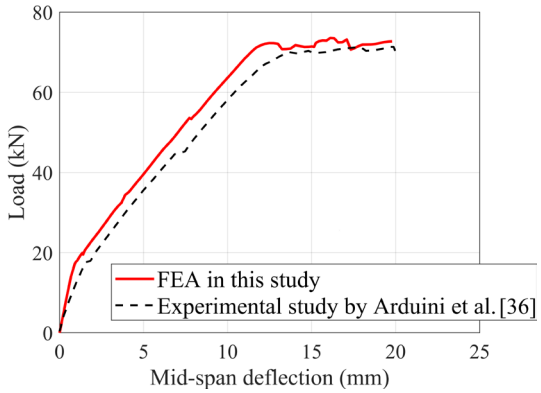

Fig. 5 Comparison of load *vs.* mid-span deflection curves

the nonlinear response following the onset of cracking and the yielding of the reinforcement. The ultimate load-carrying capacity was predicted to within close agreement of the experimental value (≈ 72 kN), demonstrating that the calibrated model satisfactorily reproduces the experimental response. The calibration of multiple constitutive parameters against a single load-deflection curve represents a consistency check rather than independent validation. The agreement obtained provides sufficient confidence in the modeling approach for the comparative parametric analyses presented in Sections 4 and 5.

4 Application of the device at the RC beam end

4.1 Structural idealization and geometric information

The structural idealization was established based on the characteristic response of a moment-resisting frame under lateral seismic loading. As shown in Fig. 6, the theoretical bending moment diagram for such frames exhibits a zero crossing near the mid-span of the beam and attains maximum values at the beam-to-column connections. Therefore, the structural model was idealized as a cantilever beam with a length corresponding to half of the clear span of the actual beam ($L_{span}/2$).

In this modeling approach, the fixed support was assigned at the location representing the beam-to-column interface. The free end corresponds to the mid-span inflection point, where the transverse load (P_{load}) representing the seismic shear demand is applied. It should be noted that the assumption of a fully fixed support does not account for the rotational flexibility of the column or the shear distortion of the joint panel zone, both of which would contribute to the total inter-story drift in a real frame. Consequently, for a given beam-end rotation, the global drift in an actual structure would be somewhat larger than the values calculated here. This idealization is justified because the present study targets the hysteretic response, energy dissipation, and damage distribution of

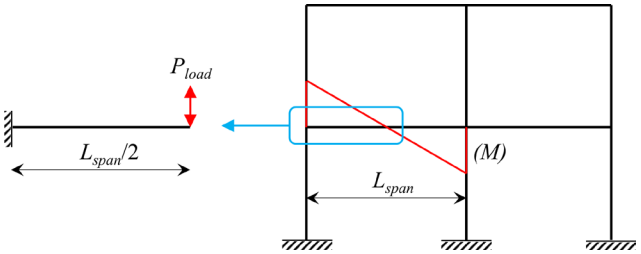

Fig. 6 Idealization of the half-span beam model from the moment distribution of a frame under lateral loading

the device-integrated RC beam in isolation, rather than the global drift response of the surrounding frame.

The geometric properties, reinforcement configuration, and finite element mesh of the reference RC beam are illustrated in Fig. 7. The beam section is rectangular, with dimensions of 250 × 500 mm and a total length of 4000 mm. To satisfy flexural requirements, the cross-section is symmetrically reinforced with six longitudinal bars of 20 mm diameter (6ϕ20) placed in both the tension and compression zones. Shear reinforcement consists of 6 mm-diameter stirrups spaced at 150 mm (ϕ6/150).

The finite element model was developed using the same meshing strategy and element types (SOLID185 for concrete and REINF264 for reinforcement) as validated in Section 3. Rigid steel plates with dimensions of 600 × 600 × 30 mm were attached at both the fixed end and the loading tip of the beam to apply boundary conditions and displacement loading without inducing localized stress concentrations. This modeling approach prevents premature local failure of the concrete at the load application points and improves convergence in the nonlinear analysis.

4.2 Integration of the device

Fig. 8 shows the finite element mesh of the device-integrated RC model. To preserve the overall model span of

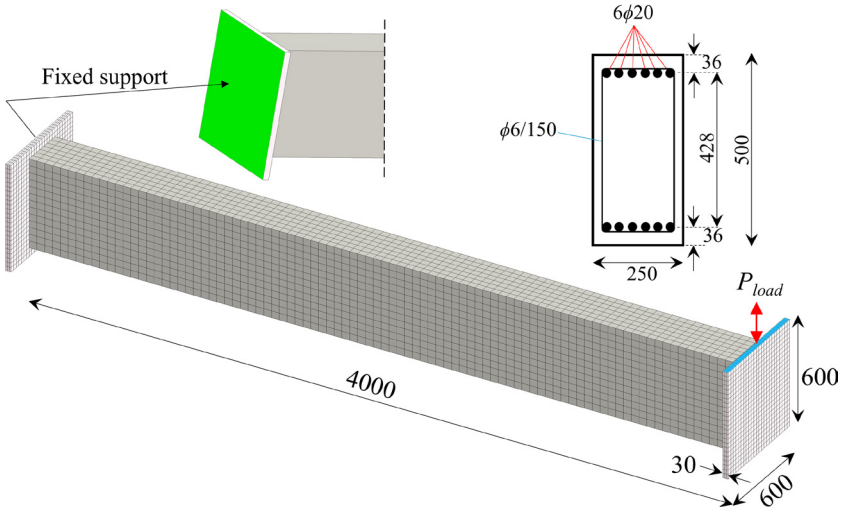

Fig. 7 Geometric details, reinforcement layout, and finite element mesh of the reference RC beam

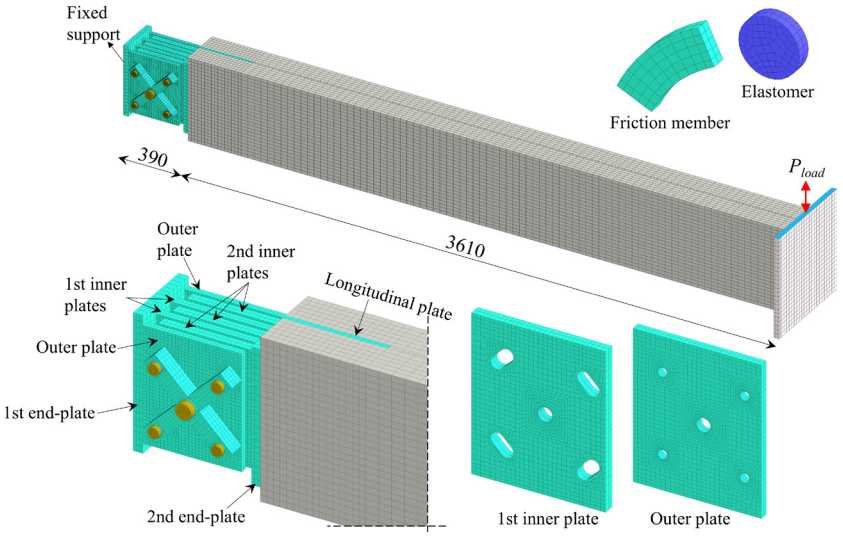

Fig. 8 Component details and finite element mesh of the device-integrated RC beam

4000 mm, the length of the RC segment was decreased by 390 mm, which matches the horizontal length of the device.

In this application, the device consists of six layers, assembled from two outer plates and five inner plates. For clarity in describing boundary conditions and force transfer, the inner plates are classified by their position: the two plates on the support side are defined as 1st inner plates, and the three plates on the RC beam side are defined as 2nd inner plates.

The 1st inner plates are welded to the 1st end-plate. In a real structure, this end-plate would be anchored to the column face; in the present model, however, the back surface of the 1st end-plate is treated as a fixed boundary, consistent with the cantilever idealization established in Section 4.1. The 2nd inner plates are welded to the 2nd end-plate, which interfaces with the RC member. A longitudinal plate is welded to the 2nd end-plate and embedded into the RC beam to transfer forces from the device to the surrounding concrete.

All steel components of the device were discretized using SOLID185 three-dimensional solid elements, consistent with the approach used for the concrete volume. For the pretensioned bolts, an M30 bolt was selected as the central master pin, with a clearance hole diameter of 33 mm. The additional bolts were specified as M20, each requiring a hole diameter of 22 mm. The thickness of both the friction members and the elastomeric pads was specified as 10 mm per layer.

The geometric specifications of the device components are detailed in Fig. 9, including the locations and radial distances of the friction members and elastomeric pads with respect to the device center, as well as the hole configurations for both the outer plate and the 1st inner plate. A semi-transparent view of the RC beam is provided to illustrate the embedment of the longitudinal plate. It should be noted that the stirrups were omitted along the embedment length (L_{long}) of the longitudinal plate, since the plate occupies the entire section depth and does not allow for a continuous vertical path for stirrup placement. In this region, shear forces are primarily transferred through the embedded plate.

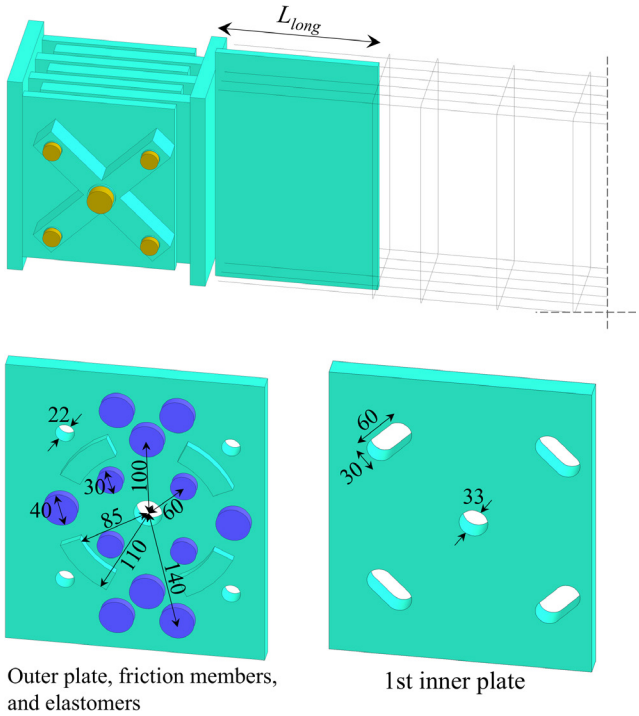

Fig. 9 Detailed dimensions of the dissipative components on the outer plate, hole configurations on the 1st inner plate, and the embedment of the longitudinal plate

Table 2 Contact pairs involving frictional interaction

Interaction group	Contact Surface 1	Contact Surface 2
Energy dissipation interface	Friction member	2nd inner plate
Plate-to-stiffness member interface	Outer plate	Stiffness member
Bolt shank-to-hole	Master pin shank / additional bolt shank	Holes of outer plate / 1st and 2nd inner plates / stiffness member / washer
Bolt head-to-washer	Bottom surfaces of master pin head / additional bolt head	Top surface of washer
Washer-to-plate	Bottom surface of washer	Stiffness member

4.3 Contact definitions and interface modeling

The friction members were modeled as bonded (welded) to the outer plates and the 1st inner plates to ensure proper alignment with these plates and uniform contact pressure across the interfaces. In contrast, between the friction members and the 2nd inner plates, a frictional contact behavior was assigned to accurately represent the sliding mechanism responsible for energy dissipation. The specific contact pairs involving frictional interaction are summarized in Table 2.

For the interaction between the 2nd end-plate and the concrete face of the RC beam, a frictionless contact model was adopted. This modeling approach ensures that the shear forces are primarily transferred through the embedded longitudinal plate rather than through surface friction at the 2nd end-plate and the concrete interface, while compressive force transfer is still permitted. All other steel-to-steel interfaces that are physically welded, such as those between inner plates and end-plates, were simulated using bonded contact definitions.

In the finite element models, a bonded contact was defined between the embedded longitudinal steel plates and the surrounding concrete. This modeling approach does not

allow for slip or separation at the steel-concrete interface. While this assumption facilitates computational convergence and simplifies the global load transfer mechanism, it represents a strong idealization. In reality, the internal force transfer between an embedded steel element and concrete is governed by complex bond-slip interactions, localized crushing, and potential interface separation under high cyclic shear and bearing stresses [37]. As a result, the local response is likely stiffer and the stress transfer more direct than in physical specimens. The response quantities reported here should be interpreted with this modeling limitation in mind. However, since all models use the same interface assumption, the comparative trends across the parameter range remain valid and provide a consistent basis for evaluating the parametric results.

For both frictional and frictionless contact pairs, the Augmented Lagrange formulation was employed in the finite element analysis. This algorithm was selected due to its robustness in nonlinear analyses, as it provides a stable solution by minimizing penetration between contact surfaces while maintaining computational efficiency.

4.4 Material properties and constitutive models

The constitutive models and material parameters for the concrete and steel reinforcement, including longitudinal bars and stirrups, were adopted identically to those described in Section 3 to maintain consistency between the validation phase and the parametric study.

Distinct material grades were assigned to the steel components of the device based on their structural roles. The steel plates and other structural components were modeled as ASTM A572 Grade 50 [38], with a nominal yield strength of 361 MPa and an ultimate tensile strength of 488 MPa. The bolts were modeled as high-strength ASTM A490 [39], with a nominal yield strength of 794 MPa and an ultimate tensile strength of 1048 MPa, consistent with the high pretension levels required to activate the friction mechanism. The cyclic response of steel was simulated using a multilinear kinematic hardening plasticity model. The von Mises yield criterion was used to define the yield surface, with a Poisson's ratio of 0.3. The stress-strain data were taken from the study by Gerami et al. [40].

The elastomeric pads were modeled as Neoprene rubber. Due to the non-linear stress-strain behavior and large deformations characteristic of rubber, a hyperelastic material formulation was required. Experimental test data, including uniaxial tension, biaxial tension, and pure shear responses, were obtained from the Ansys material library [32] and the study by Naeim and Kelly [41]. A third-order Yeoh hyperelastic model was selected to represent the material behavior, as it provides an accurate prediction of the stress-strain response over a wide deformation range. The material constants were determined by curve-fitting, minimizing the error between the numerical model and the experimental data.

The stress-strain constitutive relationships for the bolts and steel components, as well as the fitted Yeoh model curves compared with the experimental data, are presented in Fig. 10. The parameters determined for the Yeoh model are provided in Table 3.

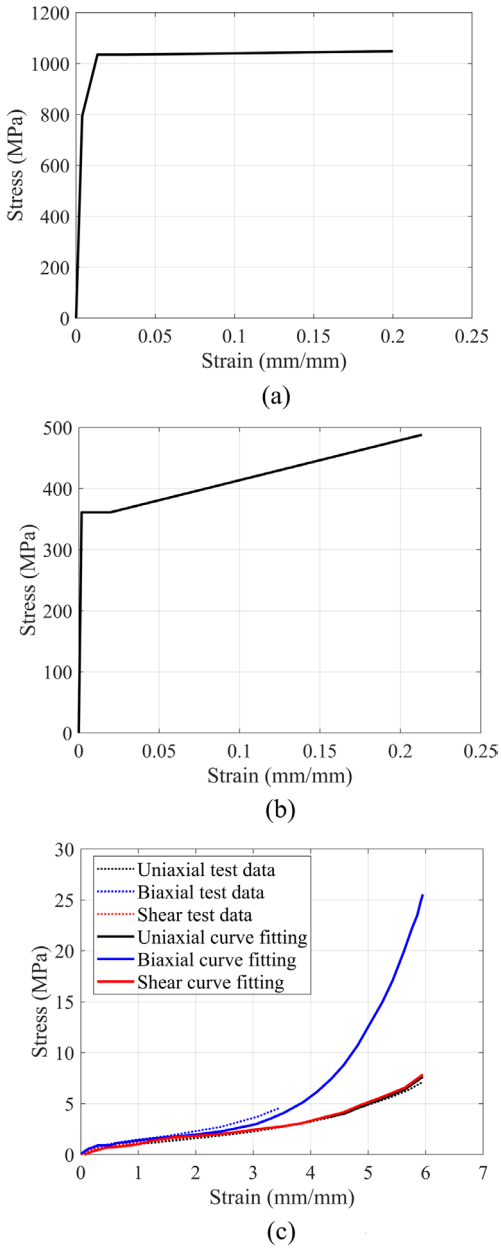

Fig. 10 Constitutive material models of stress-strain curves: (a) For bolts; (b) For steel components; (c) For elastomers, with the Yeoh model fitted to the experimental data

Table 3 The parameters for the Yeoh model (×10⁻⁴)

C_{10} (MPa)	C_{20} (MPa)	C_{30} (MPa)	D_1 (MPa)$^{-1}$	D_2 (MPa)$^{-1}$	D_3 (MPa)$^{-1}$
3614.9	−32.747	0.78785	53.653	−65.26	2.1414

4.5 Loading protocol

The numerical simulation was performed in two consecutive load steps representing the pretensioning and cyclic loading phases. In the initial step, pretension forces were applied to the master pin and the additional bolts to activate the friction mechanism and to ensure that the device components remained properly clamped throughout the subsequent loading. This procedure was implemented for all models containing the seismic device, while it was not applied to the reference RC beam, which has no prestressed components.

In the subsequent step, a cyclic displacement-controlled loading protocol was applied at the free end of the cantilever beam, as illustrated in Figs. 7 and 8. A vertical transverse displacement was imposed to induce a bending moment at the fixed support.

The loading history was developed as a simplified adaptation of the protocol specified in ANSI/AISC 341-16 standard [42], retaining the progressive drift-level structure but applying a single fully reversed cycle at each drift level rather than multiple cycles per level. The applied drift ratios were 0.375%, 0.5%, 0.75%, 1.0%, and 1.5%, respectively. The corresponding vertical displacements were determined according to the span length of the beam. This condensed loading protocol was adopted for two main reasons. First, the 3D nonlinear finite element models incorporate a large number of contact pairs with frictional and frictionless behavior, as well as hyperelastic material definitions for the elastomeric components. These features significantly increase the computational demand per load increment, making the simulation of additional drift cycles computationally prohibitive within the scope of the present parametric study. Second, the selected maximum drift ratio of 1.5% is considered representative of the primary seismic performance range for RC moment-resisting frames. Seismic design codes and guidelines for RC structures generally define interstory drift limits in the range of 1% to 2% under design-level earthquake demands [2].

4.6 Prepared models

A total of eight finite element models were prepared for the parametric study, including one reference RC beam and seven device-integrated RC beams in which the friction coefficient at the sliding interfaces, the total pretension force applied to the bolts, and both the number and length of the embedded longitudinal plates were varied. The details of the prepared models and their respective properties are presented in Table 4. The theoretical moment contributions of the friction members and elastomeric pads were calculated using Eqs. (1) to (3), based on the geometric dimensions provided in Fig. 9.

The flexural moment capacity of the reference RC beam (M_{rc}) was determined as approximately 206 kNm. This value was obtained using Eq. (4), which provides the flexural strength calculation for a doubly reinforced rectangular RC section under the assumption that the compression reinforcement remains elastic [43]. The calculation utilized the cross-sectional dimensions shown in Fig. 7 and the material properties given in Section 3.

$$M_{rc} = \left(A_s f_y - A_s' \sigma_s'\right)\left(d - a/2\right) + A_s' \sigma_s' \left(d - d'\right) \tag{4}$$

The seven device-integrated configurations were selected to span a range of relative capacities, from $M_{dev}/M_{rc} \approx 0.69$ (T600-F40-1Ls, where the device fully governs the response) to $M_{dev}/M_{rc} \approx 1.28$ (T900-F50-3L, where the device capacity exceeds that of the RC beam). This range allows the parametric study to investigate

Table 4 Prepared models and their specific properties

Model name	Friction coefficient	Pretension force (kN)	Number of longitudinal plates	Length of longitudinal plate (L_{long}) (mm)	M_F (kNm)	M_E (kNm)	M_{dev} (kNm)
RC Beam	–	–	–	–	–	–	–
T600-F40-1Ls	0.40	600	1	320	140.4	1.04	141.44
T900-F40-1Ls	0.40	900	1	320	210.6	1.04	211.64
T900-F40-1L	0.40	900	1	640	210.6	1.04	211.64
T1100-F40-1L	0.40	1100	1	640	257.4	1.04	258.44
T1100-F40-3L	0.40	1100	3	640	257.4	1.04	258.44
T1440-F30-3L	0.30	1440	3	640	252.7	1.04	253.74
T900-F50-3L	0.50	900	3	640	263.3	1.04	264.34

not only configurations consistent with capacity-design principles, but also limit cases in which the load transfer between the device and the RC member is heavily demanded, which is the regime where embedment detailing becomes most critical.

5 Results

5.1 Hysteretic response

The global moment-rotation relationships of the device-integrated RC beams under reversed cyclic loading are presented in Fig. 11, with each model shown in comparison with the reference RC beam.

The reference RC beam exhibited a conventional flexural response. After yielding of the longitudinal reinforcement, stable hysteretic loops were obtained at the early drift levels; however, the response degraded rapidly beyond approximately 0.71% drift, where severe concrete damage at the support interface led to ultimate failure. The device-integrated RC models generally produced stable and broad hysteretic loops, with their moment capacities governed by the predefined pretension forces and friction coefficients. One exception was the T900-F40-1Ls configuration, which exhibited early degradation due to localized damage in the embedment region.

To assess the consistency between the analytical capacity estimates and the numerical predictions, the maximum moment values obtained from the FE analyses ($M_{\max,FEA}$) were compared with the theoretical moment capacities (M_{rc} or M_{dev}) calculated using Eqs. (1) to (3) for the device-integrated RC beams, and Eq. (4) for the reference RC beam. The comparative results are summarized in Table 5.

To further quantify the seismic performance of the device-integrated RC models, the cumulative energy dissipation of each model was evaluated. The total energy

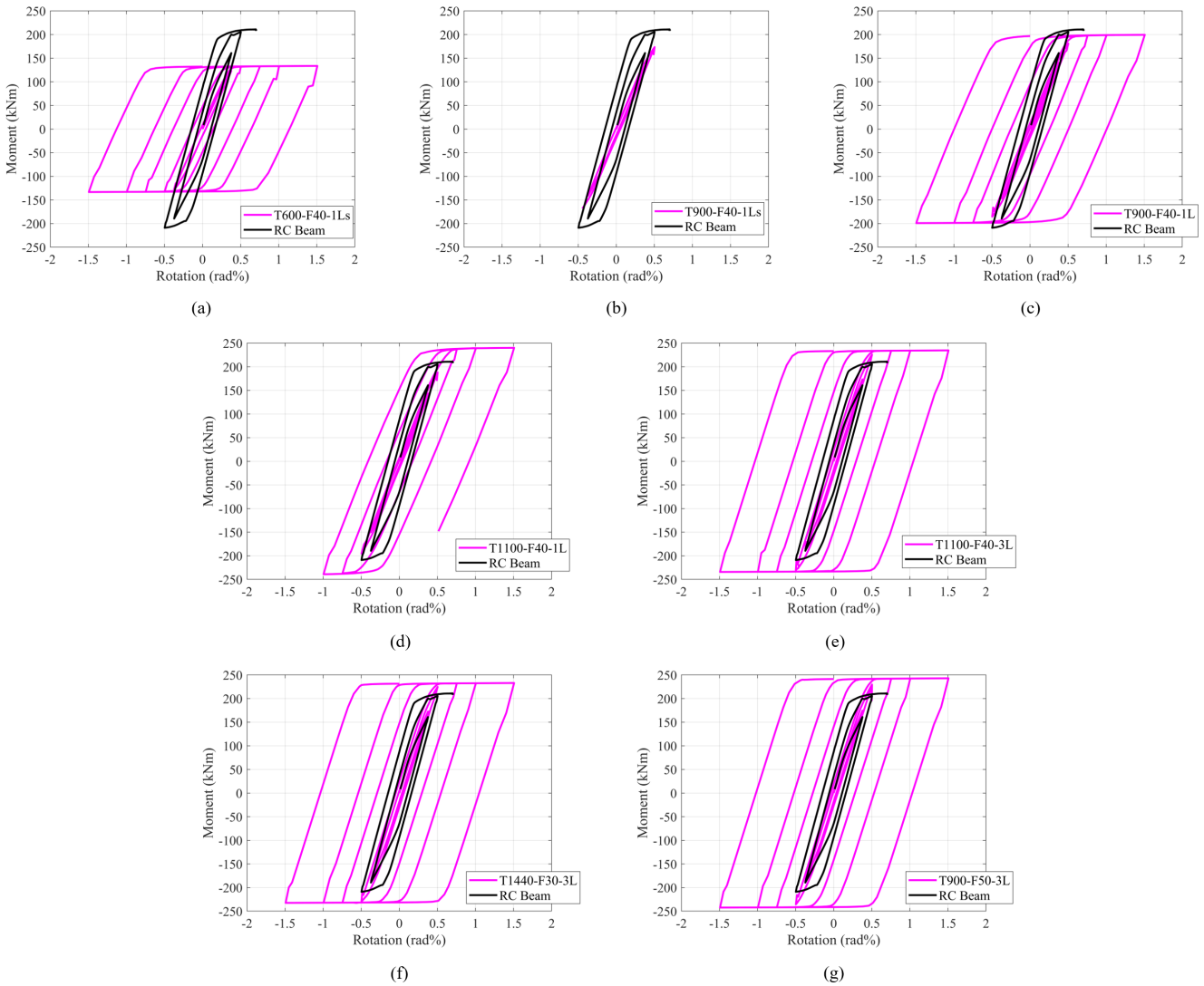

Fig. 11 The global moment-rotation relationships of the device-integrated RC models, each compared with the reference RC beam: (a) T600-F40-1Ls; (b) T900-F40-1Ls; (c) T900-F40-1L; (d) T1100-F40-1L; (e) T1100-F40-3L; (f) T1440-F30-3L; (g) T900-F50-3L

Table 5 Comparison of the theoretical moment capacities and the maximum moments obtained from the FE analyses

Model name	M_{rc} or M_{dev} (kNm)	$M_{max,FEA}$ (kNm)	Ratio
RC Beam	206	210.9	1.024
T600-F40-1Ls	141.44	133.6	0.945
T900-F40-1Ls	211.64	173.5	0.820
T900-F40-1L	211.64	199.4	0.942
T1100-F40-1L	258.44	240.1	0.929
T1100-F40-3L	258.44	234.7	0.908
T1440-F30-3L	253.74	232.9	0.918
T900-F50-3L	264.34	242.9	0.919

dissipated by the device-integrated RC model was calculated by numerically integrating the area enclosed within the moment-rotation hysteresis loops over the entire loading history. The computed cumulative energy dissipation values are displayed in Fig. 12.

The results indicate that the device-integrated configurations dissipated substantially more energy than the reference RC beam over the imposed loading history. The reference RC beam dissipated only 2.77 kNm of energy, primarily because it suffered from severe damage and reached its ultimate failure state at a relatively low drift ratio of approximately 0.71%. In contrast, the device-integrated RC models, except T900-F40-1Ls, continued to dissipate energy stably up to 1.5% drift levels.

The configuration of the longitudinal embedment plates played a critical role in the energy dissipation capacity. The models utilizing three longitudinal plates (T1100-F40-3L, T1440-F30-3L, and T900-F50-3L) consistently provided the highest energy dissipation, reaching approximately 17.4 to 17.5 kNm. By comparison, the T1100-F40-1L model with a single plate dissipated 7.99 kNm before its hysteretic loops began to degrade, while the T900-F40-1Ls

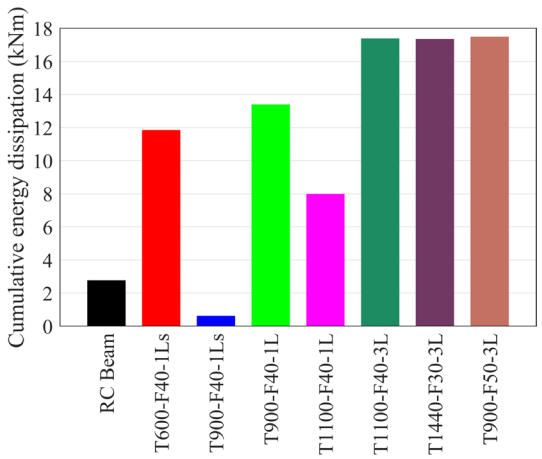

Fig. 12 Cumulative energy dissipation values

model, which had the shortest embedment length, recorded only 0.63 kNm. These results indicate that the embedment configuration strongly affects the sustained hysteretic performance of the device-integrated RC models.

5.2 Damage distribution and failure modes

The damage progression and failure modes of the analyzed models were evaluated by examining the equivalent plastic strain distributions at different loading stages. The equivalent plastic strain provides a continuum-level measure of irreversible deformation, and its spatial distribution reflects damage processes such as concrete cracking, crushing, and reinforcement yielding. Fig. 13 presents the equivalent plastic strain contours of the models at different loading stages.

For the reference RC beam, the numerical analysis indicated a conventional flexural failure characterized by severe, localized damage at the fixed support interface. During the initial loading cycles (0.375% drift), plastic deformations began to develop near the support, reaching a maximum equivalent plastic strain of approximately 0.0034. This level corresponds approximately to the plastic strain at uniaxial compressive strength of the concrete, suggesting the onset of compressive nonlinearity near the support. Concurrent yielding of the tension-side longitudinal reinforcement was also observed at this stage. As the cyclic drift increased toward the ultimate state at approximately 0.71% drift, damage became increasingly localized at the fixed support interface. At this final stage, the maximum equivalent plastic strain reached a very high value of 0.045. It is important to note that this magnitude does not represent the physical deformation capacity of the concrete material itself; rather, it is a numerical manifestation of severe strain localization.

In the device-integrated RC models, the equivalent plastic strain contours exhibited distinct patterns governed primarily by the embedment configuration of the longitudinal plates and, secondarily, by the level of pretension. In the short single-plate models (T600-F40-1Ls and T900-F40-1Ls), plastic deformations developed near the plate termination region and progressively localized within the embedment zone. This localization was particularly severe in the T900-F40-1Ls model, where the maximum equivalent plastic strain reached 0.0362 by the time the analysis terminated due to severe localization.

In the longer single-plate models (T900-F40-1L and T1100-F40-1L), extending the embedment length delayed premature damage and shifted the strain concentration

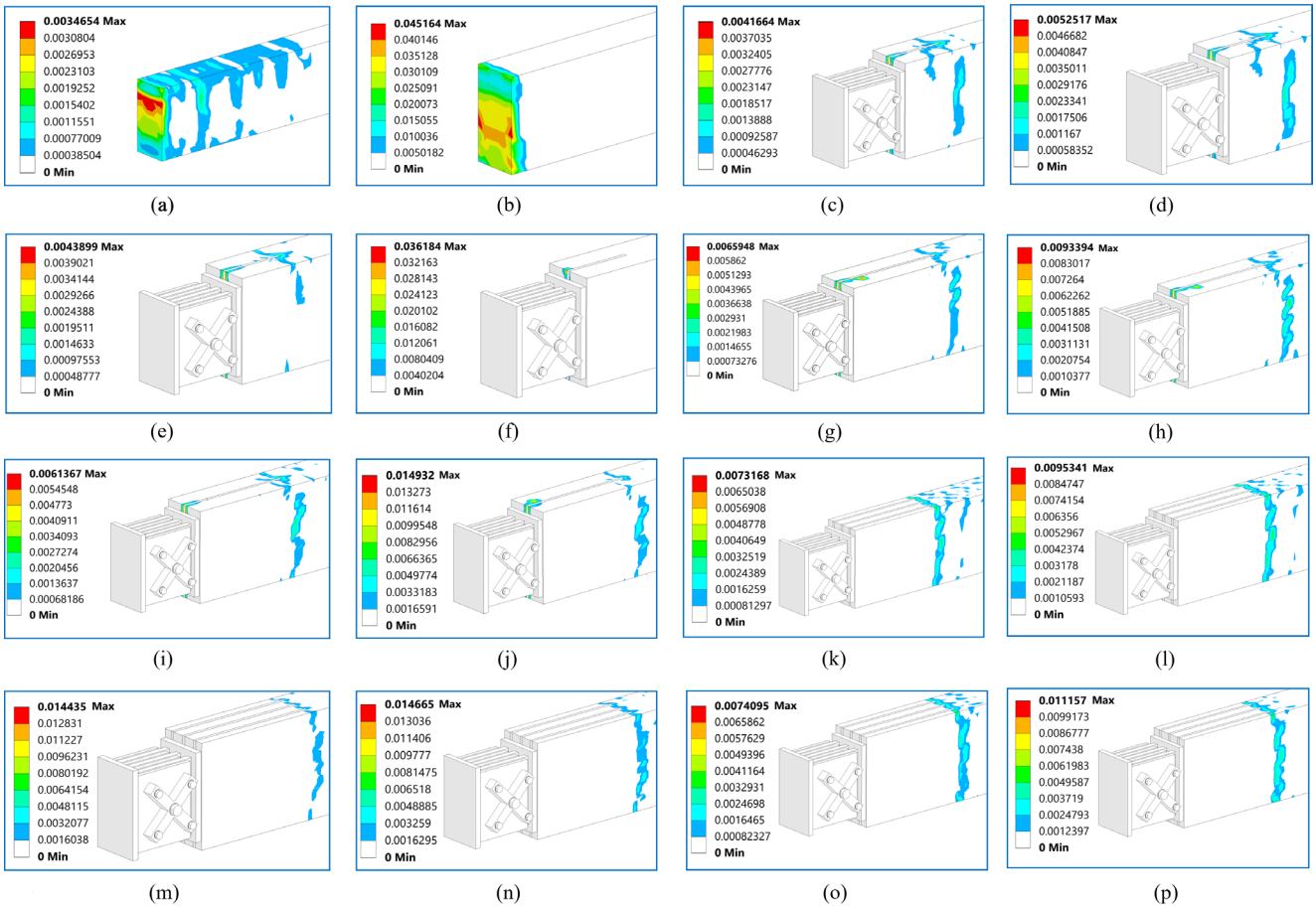

Fig. 13 Equivalent plastic strain contours of the models: (a) RC beam (−0.5 rad%); (b) RC beam (0.71 rad%); (c) T600-F40-1Ls (−0.75 rad%); (d) T600-F40-1Ls (end); (e) T900-F40-1Ls (−0.375 rad%); (f) T900-F40-1Ls (−0.48 rad%); (g) T900-F40-1L (−0.50 rad%); (h) T900-F40-1L (end); (i) T1100-F40-1L (−0.50 rad%); (j) T1100-F40-1L (1.50 rad%); (k) T1100-F40-3L (−0.50 rad%); (l) T1100-F40-3L (end); (m) T1440-F30-3L (−0.50 rad%); (n) T1440-F30-3L (end); (o) T900-F50-3L (−0.50 rad%); (p) T900-F50-3L (end)

further into the beam. Nevertheless, the plastic strain remained largely concentrated along the boundary of the single embedded plate, with maximum values of 0.0093 (T900-F40-1L) and 0.0149 (T1100-F40-1L) at the end of the loading protocol.

The multi-plate models (T1100-F40-3L, T1440-F30-3L, and T900-F50-3L) exhibited a more distributed strain pattern along the embedment region. Rather than forming a dominant localized damage zone, the plastic deformations spread across multiple vertical bands within the concrete volume. At the end of the cyclic protocol, the maximum equivalent plastic strains were 0.0095 for T1100-F40-3L, 0.0147 for T1440-F30-3L, and 0.0112 for T900-F50-3L. While these peak values are comparable to those of the long single-plate configurations, the multi-plate models exhibited the strain over multiple vertical bands rather than concentrated along a single plate boundary, indicating a more distributed damage morphology.

5.3 Force transfer in internal components of the device

The frictional forces generated in each friction member were extracted from the finite element analyses as the resultant tangential contact forces at the friction member-2nd inner plate interface, and are presented in Fig. 14. The force histories recorded during the applied loading protocol show stable and repeatable force transfer loops in all device-integrated RC models except T900-F40-1Ls. Across all configurations, a consistent difference in force magnitude was observed between the support-side and beam-side friction members. For a given bolt pretension, friction members 2 and 4 on the beam side developed higher frictional resistance than members 1 and 3 on the support side.

For example, in the T600-F40-1Ls model, the frictional forces stabilized at around 45 kN for friction members 1 and 3, while members 2 and 4 transferred approximately 60 kN. The same asymmetric distribution was also observed as the applied pretension increased. In the T1100-F40-3L

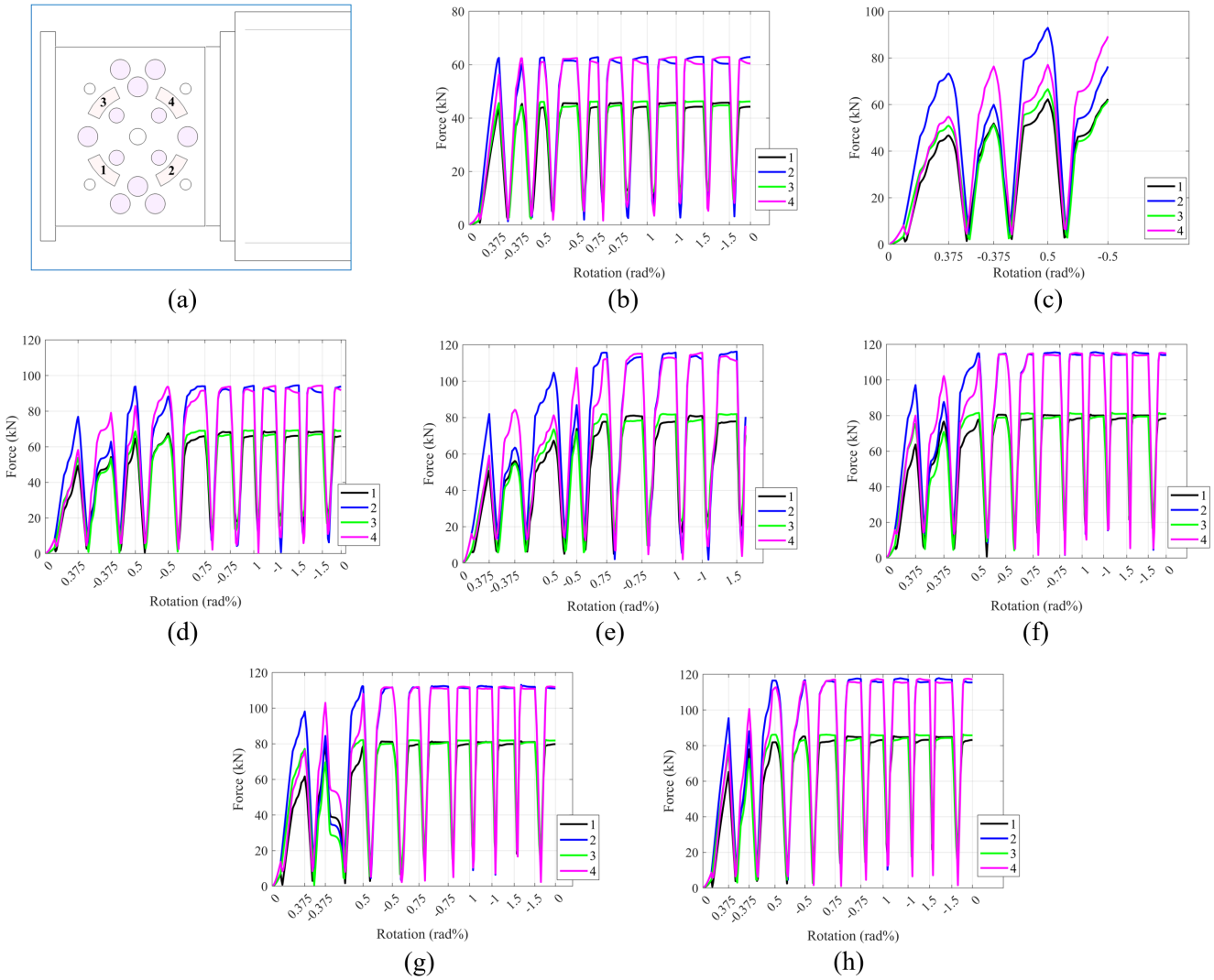

Fig. 14 The frictional forces developed within the individual friction members: (a) Friction members' number; (b) T600-F40-1Ls; (c) T900-F40-1Ls; (d) T900-F40-1L; (e) T1100-F40-1L; (f) T1100-F40-3L; (g) T1440-F30-3L; (h) T900-F50-3L

multi-plate configuration, which exhibited highly stable behavior, the maximum forces in members 1 and 3 reached about 80 kN, whereas members 2 and 4 developed frictional forces of approximately 115 kN. Comparable proportional differences were observed in the T900-F50-3L and T1440-F30-3L models, with the beam-side friction members consistently transferring higher forces than those on the support side. In contrast, the T900-F40-1Ls model showed irregular and rapidly degrading force transfer histories. In this configuration, the friction members did not sustain stable resistance throughout the loading protocol.

The force transfer histories of the elastomeric pads were also recorded to assess their contribution to the overall moment capacity, as shown in Fig. 15. According to the component layout in Fig. 9, each layer consists of 12 elastomeric pads, divided into a radially outer group (pads 1–8, 40 mm diameter) and a radially inner group (pads 9–12, 30 mm diameter). The numerical analysis indicated that the force carried by the elastomeric pads increased steadily with applied rotation, reaching maximum values at the peak drift level of 1.5%. The outer elastomers (1–8), due to their larger diameter and greater radial distance from the center of rotation, consistently developed higher resisting forces than the inner elastomers (9–12) in all models. At the maximum drift cycle, the outer pads in the multi-plate configurations reached peak forces between 0.16 kN and 0.23 kN, while the inner pads generally transferred forces below 0.08 kN. Overall, the elastomeric contribution remained small compared with that of the friction members.

6 Discussion

The numerical analyses indicate that the seismic device has promising potential for shifting a significant portion of the energy dissipation demand away from the conventional

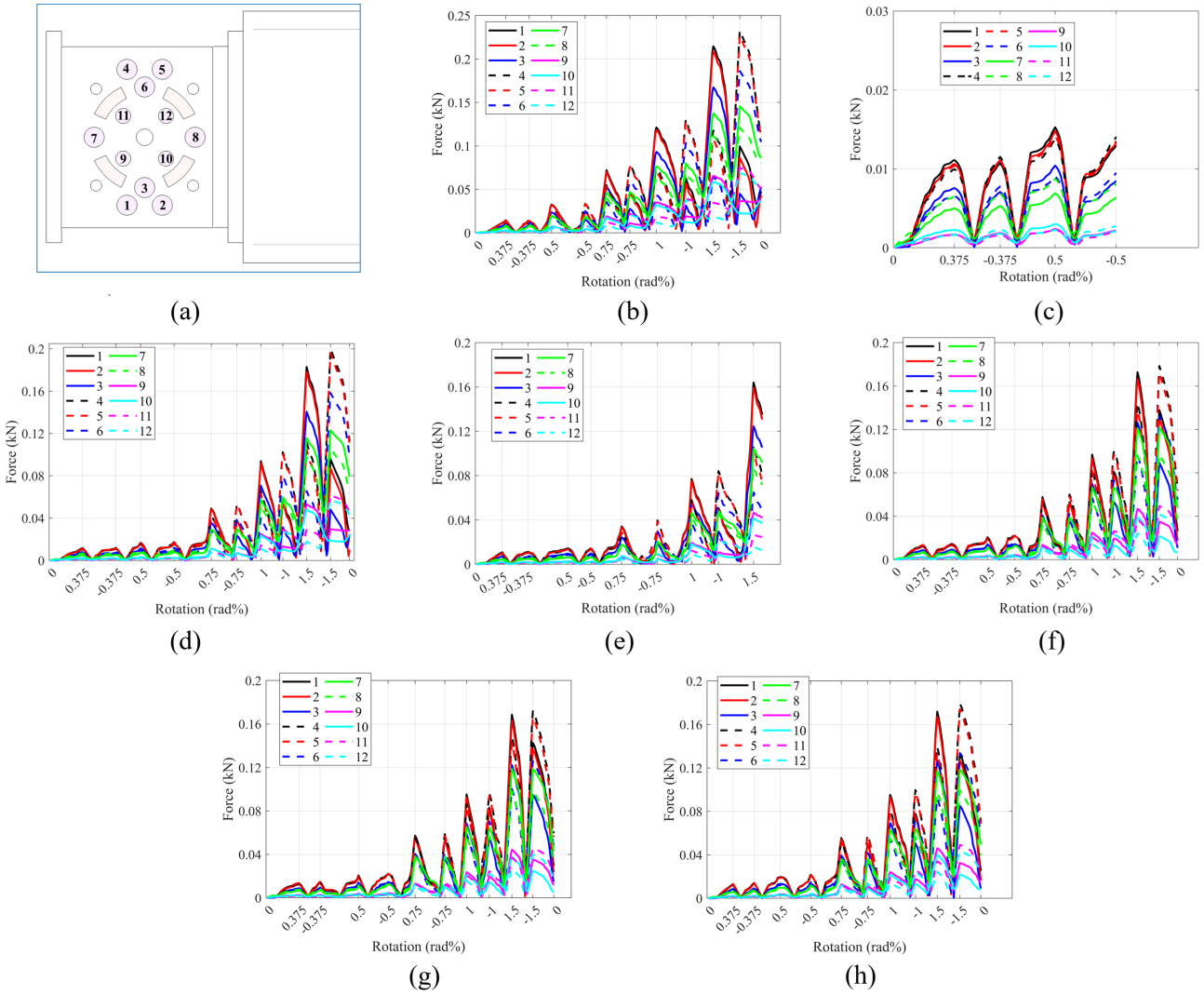

Fig. 15 The force transfer histories of the elastomeric pads: (a) Elastomers' number; (b) T600-F40-1Ls; (c) T900-F40-1Ls; (d) T900-F40-1L; (e) T1100-F40-1L; (f) T1100-F40-3L; (g) T1440-F30-3L; (h) T900-F50-3L

plastic hinge region of the RC beam. However, the results also show that this behavior is highly sensitive to the embedment configuration within the concrete and to the internal mechanisms of the device. While the damage zone was relocated away from the plastic hinge in all configurations, the extent of localized stress concentrations developed within the embedment region itself varied considerably with the embedment detailing.

6.1 Effect of embedment length and multiple plates on damage mitigation

In the reference RC beam, seismic energy dissipation occurred through significant yielding of the longitudinal reinforcement and crushing of the concrete at the beam-to-column interface, leading to severe strain localization. With the introduction of the seismic device, the dominant damage zone shifted away from this interface. However, the analyses also showed that transferring high resisting moments and shear forces from the device to the RC member may generate pronounced local stress concentrations in the embedment region. Accordingly, within the investigated parameter range, the device modified the location and distribution of damage within the RC member. This response was found to depend strongly on the embedment detailing.

Premature failure was observed in the T900-F40-1Ls model, which combines a short (320 mm) single embedded plate with a relatively high pretension level, indicating the detrimental effect of severe stress concentrations under such conditions. Localized bearing stresses at the tip of the short plate exceeded the concrete capacity in the early stages of cyclic loading, causing premature internal cracking before stable sliding could be sustained at the friction interfaces. This behavior is reflected in the extremely low energy dissipation (0.63 kNm) and the erratic force transfer

histories observed in this configuration. By contrast, the T600-F40-1Ls model with the same short embedment but a lower pretension of 600 kN remained relatively stable, suggesting that the severity of the local stress concentration, rather than the embedment length alone, governs the onset of premature failure.

When the embedment length was extended to 640 mm, as in the T900-F40-1L, premature failure was delayed due to the increased development length for shear transfer. However, the use of a single longitudinal plate continued to restrict force transfer to a single plane within the beam cross-section. Under high pretension forces in the T1100-F40-1L, this single-plane transfer led to localized yielding of the concrete along the plate boundary, as indicated by progressive strain localization at larger drift ratios.

The adoption of a multi-plate embedment configuration, as in the 3L models, was found to be the most effective strategy for damage mitigation within the investigated parameter range. The use of three longitudinal plates allowed the internal shear and bearing forces to be distributed over a larger volume of the concrete core, thereby redistributing the localized bearing stresses and limiting severe crushing or widespread cracking. As a result, the damage morphology shifted from highly localized failure planes to a more uniformly distributed crack pattern, represented by vertical strain bands. This distributed force transfer mechanism enabled the friction components to sustain stable sliding over multiple cycles at high drift ratios and led to the highest cumulative energy dissipation values among the examined configurations.

6.2 Behavior of the friction and elastomeric components

The force transfer histories within the internal components revealed an asymmetric distribution of frictional forces between the support-side and beam-side friction members, which warrants closer examination. It was consistently observed that the frictional resistance developed by the friction members on the fixed support side (members 1 and 3) was lower than that of the friction members on the beam side (members 2 and 4).

This difference in frictional resistance is primarily due to the geometric and boundary conditions of the device assembly. Specifically, the outer plate on the fixed support side is welded directly to the 1st end-plate, which restricts its ability to deform inward when the master pin and additional bolts are pretensioned. As a result, the welded constraint suppresses the flexural deformation of this outer plate, which limits the transmission of the pretension force as normal pressure onto friction members 1 and 3. In contrast, the outer plate on the beam side is able to deform inward under bolt pretension, allowing a greater normal force to be applied to friction members 2 and 4. This asymmetry in boundary conditions results in higher resisting forces in the beam-side friction members.

The forces resisted by the elastomeric pads were significantly lower than those carried by the friction members in all configurations. This outcome is directly related to the limited drift range of the applied loading protocol (up to 1.5%), which was selected to investigate the basic behavior of the device within the primary seismic performance range for RC moment-resisting frames. Unlike the friction members, the elastomeric components contribute to the moment capacity through an elastic mechanism. Their contribution scales linearly with the imposed rotation (Eq. (2)). Within the drift range examined here, this rotation was insufficient to fully mobilize the elastomeric components, and their moment contribution remained modest relative to the frictional component. However, the elastomeric contribution grows in absolute terms at larger rotations and is expected to become more relevant in applications imposing substantially higher drift demands, including the original steel frame application for which the device was developed [31].

7 Limitations and future research

The numerical models developed in this study provide detailed insight into the stress distribution and energy dissipation mechanisms of the proposed configuration; however, several idealizations were necessarily adopted. Two of these idealizations are related to the force-transfer conditions in the embedment zone, while a third concerns the internal mechanics of the device itself:

1. First, the bonded contact assumed between the embedded longitudinal steel plates and the surrounding concrete (Section 4.3) represents a significant simplification of the actual steel-concrete interface, which in practice exhibits bond-slip, localized crushing, and potential separation under cyclic loading [37]. Future numerical studies should incorporate cohesive zone or bond-slip interface models to capture these effects, especially the force redistribution along the embedment region and the progressive interface damage that the present model cannot represent.
2. Second, stirrups were omitted along the embedment length of the longitudinal plate. The reason is geometric: the embedment depth of the longitudinal

plate equals the full depth of the RC beam, leaving no transverse path for stirrups to traverse the section. A shorter plate depth would create space for stirrups, but would also concentrate severe stresses in the concrete above and below the plate, undermining the embedment. Although the embedded plate is expected to transfer shear forces within this region, the absence of transverse reinforcement removes the lateral confinement and crack-width control normally provided by stirrups. A single concrete material model was used throughout, without an explicit distinction between confined and unconfined zones; the local damage observed in this region should therefore be regarded as an idealized estimate. Future studies may investigate alternative geometric configurations that permit the inclusion of stirrups within the embedment region, such as connecting the 2nd end-plate to the RC beam through anchor bars instead of an embedded longitudinal plate.

3. Third, a simplification concerns the device itself. The present finite element models assume a constant friction coefficient and a fixed bolt pretension force throughout the entire loading history. Preliminary laboratory tests of the device in its standalone form have been reported in Yılmaz et al. [44] and Bekiroğlu et al. [45]. These tests indicated that the device could achieve the targeted moment capacity and dissipate energy without yielding. However, under extended cyclic loading, friction-induced wear at the sliding interfaces led to a reduction in bolt pretension and a gradual decrease in moment-carrying capacity. Subsequent design iterations of the device (not included in the present numerical models) incorporated surface-hardening treatments for the 2nd inner plates and Belleville washers (disc springs) arranged in series and parallel along the pretensioned bolts, which improved the stability of the clamping force and the consistency of the moment capacity over repeated cycles. These refinements were beyond the scope of the present study, which focuses on the fundamental hysteretic behavior of the device-integrated concept under idealized conditions.

Beyond these modeling considerations, the practical implementation of the device in RC members introduces additional challenges regarding replaceability. The seismic device was originally developed as a replaceable structural fuse intended to protect the main load-bearing members from damage, and this objective has been demonstrated in steel beam-to-column applications. In the present RC application, however, the degree of protection achieved in the main structural member was strongly configuration-dependent. For example, the T600-F40-1Ls model has a device-to-beam moment capacity ratio of approximately 0.69, which satisfies capacity-design principles. Nevertheless, localized concrete damage still developed in the embedment region due to the short embedment length, demonstrating that protection depends not only on the global capacity ratio but also on the local force-transfer detailing. Therefore, the post-earthquake replaceability of the device in RC applications is expected to depend strongly on the local detailing and on the extent of damage developed in the embedment region.

Future research should focus on comprehensive experimental testing of the device integrated within an RC element. Such tests are necessary to evaluate bond-slip behavior, local concrete damage, internal force-transfer mechanisms, and the overall cyclic interaction between the embedded longitudinal plate and the surrounding RC member. In parallel, future numerical studies should incorporate explicit transverse reinforcement detailing within the embedment zone (where geometric configurations permit) to better capture confinement effects and crack morphology. They should also consider modeling the progressive reduction in bolt pretension due to interface wear, in order to more accurately represent long-term cyclic performance.

8 Conclusions

The numerical results of this study indicate that integrating a frictional and elastomeric seismic device into an RC beam is a promising yet detail-sensitive strategy for low-damage seismic design. Rather than concentrating solely at the conventional plastic hinge, a significant portion of the dissipative action is transferred to the internal components of the device. Based on the numerical evaluations, the following conclusions are drawn:

- The results indicate that the concept promotes a redistribution of internal forces and damage within the device-integrated RC system, with improved structural performance obtained when the embedment details enable a more distributed force-transfer mechanism. When resisting forces are applied through inadequate embedment details, significant local stress concentrations are observed. Therefore, the structural performance of the device-integrated RC system depends not only on the nominal capacity of the device but, equally importantly, on the effectiveness of the local force-transfer mechanism.

- The results further demonstrate that distributing internal forces over a larger concrete volume, rather than concentrating them in a single plane, allows the friction mechanism to remain stable over more loading cycles, thereby substantially increasing the cumulative energy dissipation capacity. The use of multi-plate configurations resulted in increased cumulative energy dissipation and a more distributed damage pattern within the concrete core, rather than severe strain localization.
- The total moment capacity and energy dissipation of the device were primarily governed by the frictional components, whereas the moment contribution from the elastomeric pads remained limited within the deformation range considered in this study. This limited contribution is attributed to the imposed drift level rather than to the inherent capacity of the elastomers; their elastic moment contribution scales linearly with rotation and is expected to become more relevant at substantially larger drift levels.

All conclusions presented above are based exclusively on numerical simulations; the device-integrated concept has not yet been experimentally verified in an RC element. The present results provide a numerically supported feasibility assessment, identifying the critical design parameters that should guide future experimental investigations: namely the embedment detailing and the local force-transfer mechanisms.

Declaration of competing interest

The frictional and elastomeric seismic device investigated in this study is protected by a patent registered at the Turkish Patent and Trademark Office (TÜRKPATENT) under registration number TR 2020 18195. The applicant of the patent is Yildiz Technical University, and Orkun Yılmaz and Serkan Bekiroğlu are the inventors. A related European patent application is also currently under examination before the European Patent Office (EPO). A related U.S. patent application was previously filed but is no longer active.

Among the authors of this manuscript, Orkun Yılmaz is a co-inventor of the patent and therefore declares a potential competing interest with respect to the commercialization of the device. Lal Oğuz declares no competing interests. No other competing interests, financial or non-financial, are declared.

Declaration of generative AI in the manuscript preparation process

During the preparation of this manuscript, the authors used AI-assisted tools (Claude, Anthropic) to support language editing, improve readability and clarity. All scientific content, analyses, and conclusions are the responsibility of the authors, who reviewed and edited all suggestions and take full responsibility for the final content of the publication.

Acknowledgements

This article is based on a part of the ongoing MSc research of Lal Oğuz at Yildiz Technical University.

The authors gratefully acknowledge Prof. Serkan Bekiroğlu for insightful discussions and constructive feedback during various stages of this study.

This research did not receive any specific grant from funding agencies in the public, commercial, or not-for-profit sectors.

References

[1] Paulay, T., Priestley, M. J. N. "Seismic Design of Reinforced Concrete and Masonry Buildings", John Wiley & Sons, Inc., 1992. ISBN 9780470172841 https://doi.org/10.1002/9780470172841

[2] Fardis, M. N. "Seismic Design, Assessment and Retrofitting of Concrete Buildings: Based on EN-Eurocode 8", Springer Dordrecht, 2009. ISBN 978-1-4020-9842-0 https://doi.org/10.1007/978-1-4020-9842-0

[3] Soydan, C., Özkaynak, H., Sürmeli, M., Şenol, E., Saruhan, H., Yüksel, E. "A moment resistant beam end connection using energy dissipative couplers for precast concrete structures", Bulletin of Earthquake Engineering, 23(1), pp. 453–487, 2025. https://doi.org/10.1007/s10518-024-02067-9

[4] Colajanni, P., La Mendola, L., Monaco, A., Pagnotta, S. "Low-Damage Friction Connections in Hybrid Joints of Frames of Reinforced-Concrete Buildings", Applied Sciences, 13(13), 7876, 2023. https://doi.org/10.3390/app13137876

[5] Qu, X., Qin, C., Sun, G., Deng, Y., Fu, X. "Seismic behavior of precast prestressed concrete frame joints with different energy dissipation designs", Advances in Structural Engineering, 27(1), pp. 51–71, 2024. https://doi.org/10.1177/13694332231213455

[6] Sonda, D., Pollini, A. V. "TH Analyses and Simplified Approach for Precast RC Frames Retrofit with Dissipative Fuse Devices Sismocell", Procedia Structural Integrity, 44, pp. 1188–1195, 2023. https://doi.org/10.1016/j.prostr.2023.01.153

[7] El-Bahey, S., Bruneau, M. "Structural Fuse Concept for Bridges", Transportation Research Record: Journal of the Transportation Research Board, 2202(1), pp. 167–172, 2010. https://doi.org/10.3141/2202-20

[8] Dutta, A., Mander, J. B. "Seismic design for damage control and repairability", In: 8th US National Conference on Earthquake Engineering 2006, San Francisco, CA, USA, 2006, pp. 9563–9572. ISBN 9781615670444

[9] Dougka, G., Dimakogianni, D., Vayas, I. "Innovative energy dissipation systems (FUSEIS 1-1) — Experimental analysis", Journal of Constructional Steel Research, 96, pp. 69–80, 2014. https://doi.org/10.1016/j.jcsr.2014.01.003

[10] Pratap, M., Vesmawala, G. R. "An experimental and numerical analysis of slit plate as replaceable fuse in moment resisting frame", Structures, 67, 107011, 2024. https://doi.org/10.1016/j.istruc.2024.107011

[11] Nguyen, T. N., Eatherton, M. R. "Computational and experimental study of structural fuses optimized to resist buckling", Journal of Constructional Steel Research, 201, 107688, 2023. https://doi.org/10.1016/j.jcsr.2022.107688

[12] Farzampour, A. "Structural behavior prediction of the Butterfly-shaped and straight shear fuses", Structures, 33, pp. 3964–3972, 2021. https://doi.org/10.1016/j.istruc.2021.07.008

[13] Avecillas, J. A., Eatherton, M. R. "Topology optimization of steel shear fuses to resist buckling", In: Proceedings of the Annual Stability Conference Structural Stability Research Council, St. Louis, MO, USA, 2019, pp. 1–11. ISBN 978-1-5108-8446-5

[14] Goshtaei, S. M., Moradi, S., Hossain, K. M. A. "Multi-objective optimization of energy-dissipating steel plate fuse links using response surface method", Structures, 62, 106224, 2024. https://doi.org/10.1016/j.istruc.2024.106224

[15] Eatherton, M. R., Nguyen, T. N. "Structural fuse shapes for resilient structures", In: 18th World Conference on Earthquake Engineering, Milan, Italy, 2024, pp. 1–12. ISBN 9798331314910

[16] Ferraioli, M., Mottola, S., Mistakidis, E., De Matteis, G. "Lateral torsional buckling design of dumbbell-shaped steel strip dampers", Structures, 77, 109080, 2025. https://doi.org/10.1016/j.istruc.2025.109080

[17] Sarkisian, M. P. "Building systems using seismic fuses with advanced material and friction", In: Li, C.-Q., Frangopol, D. M. (eds.) Life-Cycle Performance of Structures and Infrastructure Systems in Diverse Environments, CRC Press, 2025, pp. 302–309. ISBN 9781003595120 https://doi.org/10.1201/9781003595120-36

[18] Latour, M., Piluso, V., Rizzano, G. "Experimental analysis of beam-to-column joints equipped with sprayed aluminium friction dampers", Journal of Constructional Steel Research, 146, pp. 33–48, 2018. https://doi.org/10.1016/j.jcsr.2018.03.014

[19] Cui, Y., Yan, Z., Wang, X., Wang, T. "Experimental studies on slip friction device using symmetric friction connections", Structures, 44, pp. 1886–1897, 2022. https://doi.org/10.1016/j.istruc.2022.09.005

[20] Yang, C., Xie, L., Li, A., Liu, B., He, Y. "Experimental study of rotational friction damper for seismic response control: Friction material comparison and configuration optimization", Case Studies in Construction Materials, 21, e03825, 2024. https://doi.org/10.1016/j.cscm.2024.e03825

[21] Bozer, A., Özgan, H., Yıldız, N. "A Novel Friction-Based Energy Dissipation System for Seismic Applications", In: 3rd International Workshop on Energy-Based Seismic Engineering, Istanbul, Türkiye, 2025, pp. 325–337. ISBN 978-3-031-97129-7 https://doi.org/10.1007/978-3-031-97129-7_26

[22] Chan, R. W. K., Tang, W. "Serviceability conditions of friction dampers for seismic risk mitigations", Structures, 35, pp. 500–510, 2022. https://doi.org/10.1016/j.istruc.2021.11.033

[23] Lomiento, G., Bonessio, N., Benzoni, G. "Friction Model for Sliding Bearings under Seismic Excitation", Journal of Earthquake Engineering, 17(8), pp. 1162–1191, 2013. https://doi.org/10.1080/13632469.2013.814611

[24] Sarkisian, M., Mathias, N., Garai, R., Horiuchi, C. "Improving Seismic Resilience Using Structural Systems with Friction-based Fuses", In: AEI 2017, Oklahoma City, OK, USA, 2017, pp. 591–602. ISBN 9780784480502 https://doi.org/10.1061/9780784480502.049

[25] Shahbazi, B., Moaddab, E. "A New Hybrid Friction Damper (HFD) for Dual-Level Performance of Steel Structures", International Journal of Steel Structures, 21(4), pp. 1332–1345, 2021. https://doi.org/10.1007/s13296-021-00507-9

[26] Soltani, S., Javaheri-tafti, M. R., Vetr, M. G. "Numerical Investigation of Pinned Fuse with Simple Replacing in Steel Eccentrically Braced Frames and Design Parameters Determination", Journal of Rehabilitation in Civil Engineering, 12(2), pp. 97–110, 2024. https://doi.org/10.22075/jrce.2023.28997.1752

[27] He, X., Ke, K., Guo, L., Yam, M. C. H., Wang, Z. "A replaceable fuse steel-concrete composite connection: Force transfer mechanism and design considerations", Journal of Constructional Steel Research, 183, 106760, 2021. https://doi.org/10.1016/j.jcsr.2021.106760

[28] Richards, P. "A repairable connection for earthquake-resisting moment frames", Steel Construction, 12(3), pp. 191–197, 2019. https://doi.org/10.1002/stco.201900015

[29] Tian, J., Wang, Z., Pan, J. "Research on design guidelines for steel beam-to-column connections with replaceable buckling-restrained fuse plates", Journal of Constructional Steel Research, 232, 109622, 2025. https://doi.org/10.1016/j.jcsr.2025.109622

[30] Lignos, D. G., Paronesso, M. "Low-damage steel structures for enhanced life-cycle seismic performance", Stahlbau, 91(5), pp. 315–325, 2022. https://doi.org/10.1002/stab.202200023

[31] Yılmaz, O. "Depreme Dayanıklı Çelik Çerçevelerde Hasar Alan veya Almayan Yüksek Enerji Tüketen Moment Birleşimlerinin Geliştirilmesi" (Development of Damaged or Non-damaged High Energy Dissipative Moment Connections in Seismic Resistant Steel Frames), PhD Thesis, Yildiz Technical University, 2022. (in Turkish)

[32] ANSYS, Inc. "Ansys Academic Research Mechanical, (Release 2024 R2)", [computer program] Available at: https://www.ansys.com [Accessed: 10 January 2025]

[33] Yılmaz, O., Bekiroğlu, S. "Bilhassa binalarda kullanılmak üzere sürtünmeli ve elastomerli sismik birleşim aparatı" (A seismic combination apparatus with elastomer and with friction particularly for use in buildings), Turkish Patent and Trademark Office, Ankara, Türkiye, Patent No: TR 2020 18195, 2024. (in Turkish)

[34] Yılmaz, O., Bekiroğlu, S. "Development of a Frictional and Elastomeric Seismic Joint Apparatus for Use in Buildings", In: 14th International Congress on Advances in Civil Engineering (ACE 2020-21), Istanbul, Türkiye, 2021, pp. 260–267.

[35] Yılmaz, O., Bekiroğlu, S. "The frictional and elastomeric seismic joint apparatus and its usage as a steel beam-to-column connection", In: 3rd International Civil Engineering and Architecture Congress (ICEARC'23), Trabzon, Türkiye, 2023, pp. 970–979. ISBN 978-605-81854-7-0. https://doi.org/10.31462/icearc.2023.sme137

[36] Arduini, M., Di Tommaso, A., Nanni, A. "Brittle Failure in FRP Plate and Sheet Bonded Beams", Structural Journal, 94(4), pp. 363–370, 1997. https://doi.org/10.14359/487

[37] Eligehausen, R., Popov, E. P., Bertero, V. V. "Local bond stress-slip relationships of deformed bars under generalized excitations: experimental results and analytical model", College of Engineering, University of California, Berkeley, CA, USA, Rep. UCB/EERC-83/23, 1983. [online] Available at: https://nehrpsearch.nist.gov/static/files/NSF/PB84192848.pdf [Accessed: 13 March 2026]

[38] ASTM International "ASTM A572/A572M-12 Standard Specification for High-Strength Low-Alloy Columbium-Vanadium Structural Steel", ASTM International, West Conshohocken, PA, USA, 2012. https://doi.org/10.1520/A0572_A0572M-12

[39] ASTM International "ASTM F3125/F3125M-22 Standard Specification for High Strength Structural Bolts and Assemblies, Steel and Alloy Steel, Heat Treated, Inch Dimensions 120 ksi and 150 ksi Minimum Tensile Strength, and Metric Dimensions 830 MPa and 1040 MPa Minimum Tensile Strength", ASTM International, West Conshohocken, PA, USA, 2022. https://doi.org/10.1520/F3125_F3125M-22

[40] Gerami, M., Saberi, H., Saberi, V., Daryan, A. S. "Cyclic behavior of bolted connections with different arrangement of bolts", Journal of Constructional Steel Research, 67(4), pp. 690–705, 2011. https://doi.org/10.1016/j.jcsr.2010.11.011

[41] Naeim, F., Kelly, J. M. "Design of Seismic Isolated Structures: From Theory to Practice", John Wiley & Sons, Inc., 1999. ISBN 9780470172742 https://doi.org/10.1002/9780470172742

[42] AISC "ANSI/AISC 341-16, Seismic Provisions for Structural Steel Buildings", American Institute of Steel Construction, Chicago, IL, 2016.

[43] Doğangün, A. "Betonarme Yapıların Hesap ve Tasarımı" (Calculation and Design of Reinforced Concrete Structures), Birsen Yayınevi, 2020. ISBN 9789755113104 (in Turkish)

[44] Yılmaz, O., Bekiroğlu, S., Alemdar, F., Yılmaz, M. O., Fırat Alemdar, Z., Sevim, B., Arslan, G., Ayvaz, Y. "Geliştirilen bir sismik birleşim aparatının kismî prototip testleri" (Partial prototype tests of a developed seismic connection apparatus), In: 9th Structural Mechanics Laboratories Workshop, Düzce, Türkiye, 2024, pp. 155–160. (in Turkish)

[45] Bekiroğlu, S., Ayvaz, Y., Arslan, G., Sevim, B., Alemdar, F., Fırat Alemdar, Z., Yılmaz, O., Yılmaz, M.O. "Simülasyon ortamında geliştirilen sürtünmeli ve elastomerli sismik birleşim aparatının kismi prototip testleri" (Partial Prototype Tests of a Friction and Elastomeric Seismic Joint Device Developed in a Simulation Environment), Yildiz Technical University Scientific Research Projects Coordination Unit, Istanbul, Türkiye, Rep. FBA-2022-5013, 2026. (in Turkish)